

Synthesis of sub-5 nm Co-doped SnO₂ nanoparticles and their structural, microstructural, optical and photocatalytic properties

T. Entradas¹, J. Cabrita¹, S. Dalui², M.R. Nunes¹, O.C. Monteiro^{1*} and A.J. Silvestre^{3*}

¹Department of Chemistry and Biochemistry and CQB, Faculty of Sciences, University of Lisbon, Campo Grande, 1749-016 Lisboa, Portugal.

²Department of Physics and ICEMS, Faculty of Sciences, University of Lisbon, Campo Grande, 1749-016 Lisboa, Portugal.

³Department of Physics and ICEMS, Instituto Superior de Engenharia de Lisboa - ISEL, R. Conselheiro Emídio Navarro 1, 1959-007 Lisboa, Portugal.

ABSTRACT

A swift chemical route to synthesize Co-doped SnO₂ nanopowders is described. Pure and highly stable Sn_{1-x}Co_xO_{2-δ} ($0 \leq x \leq 0.15$) crystalline nanoparticles were synthesized, with mean grain sizes < 5 nm and the dopant element homogeneously distributed in substitutional sites of the SnO₂ matrix. The UV-visible diffuse reflectance spectra of the Sn_{1-x}Co_xO_{2-δ} samples reveal red shifts, the optical bandgap energies decreasing with increasing Co concentration. The samples' Urbach energies were calculated and correlated with their bandgap energies. The photocatalytic activity of the Sn_{1-x}Co_xO_{2-δ} samples was investigated for the 4-hydroxybenzoic acid (4-HBA) degradation process. A complete photodegradation of a 10 ppm 4-HBA solution was achieved using 0.02% (w/w) of Sn_{0.95}Co_{0.05}O_{2-δ} nanoparticles in 60 min of irradiation.

Keywords: Co-doped SnO₂ nanoparticles; Optical bandgap; Urbach energy, Photocatalysis, 4-hydroxybenzoic acid (4-HBA).

*Authors to whom correspondence should be addressed: Telephone: +351-217500865, Fax: +351-217500088, Email: ocmonteiro@fc.ul.pt (O.C. Monteiro); Telephone: +351-218317097, Fax: +351-21837138, Email: asilvestre@deq.isel.ipl.pt (A.J. Silvestre).

1. INTRODUCTION

Tin dioxide (SnO_2) is a wide bandgap metal oxide semiconductor in which inherent oxygen vacancies act as *n*-type dopants [1,2]. It has a *rutile*-type tetragonal structure based on octahedra wherein each tin atom is surrounded by six oxygen atoms, and its space group is $P_{42/mnm}$. The standard lattice parameters are $a = b = 4.7382 \text{ \AA}$ and $c = 3.1871 \text{ \AA}$ [3]. At room temperature SnO_2 has an optical bandgap of $\sim 3.6 \text{ eV}$ [4,5]. From the applications point of view, SnO_2 has been investigated in a broad variety of fields, including gas, *pH* and bio-sensors [6-11], transparent conducting electrodes [12,13], lithium ion batteries [14,15], field effect transistors [16], sensitized solar cells [17,18] and varistors [19]. SnO_2 has also been used in catalysis, as metal oxide support for precious metal catalysts in systems such as Pt/SnO_2 , Pd/SnO_2 , Ru/SnO_2 and Rh/SnO_2 [20], for the combustion at low temperatures of volatile organic compounds. Moreover, Co-doped SnO_2 has gained immense interest, being one of the first oxide-based diluted magnetic semiconductor (DMS) systems to be investigated [21], in parallel with the Co:TiO_2 [22,23] and Co:ZnO [24] systems, exhibiting ferromagnetic order well above room temperature.

The use of SnO_2 in photocatalysis has been much less studied, despite its crystalline structure being very similar to that of TiO_2 , a worldwide used photocatalyst [25]. Indeed, a crystal network of corner-sharing octahedral units is considered as a pre-requisite for high photocatalytic activity since such a network increases the mobility of electrons and holes and consequently affects the probability of electrons and holes reaching the reaction sites on the surface of the photocatalyst [26]. Besides the crystal structure, a good photocatalyst should also have an adequate absorption band and a high specific surface area. The former property can be achieved, for instance, by tailoring the optical bandgap through doping [27], and the latter by controlling the particle size. However, it is still a challenge to prepare semiconductor nanocrystals with controllable size, shape and doping. In particular, the synthesis of nanoparticles of sizes under 10 nm still remains a major challenge [28]. They usually require complex synthesis procedures and/or suffer problems of aggregation or poor monodispersity, which strongly influence their properties and restrict their large-scale industrial production.

This work reports on a swift chemical route to synthesise highly stable undoped and Co-doped SnO_2 nanoparticles, with different dopant concentrations and grain sizes below 5 nm. The synthesis procedure is highly reproducible, low-cost and easily scaled-up. The influence of the Co doping concentration on the structure, microstructure and optical properties of the different synthesized samples was studied. The potential applicability of these materials for

organic pollutant remediation processes was investigated, by studying their photocatalytic performance in the 4-hydroxybenzoic acid (4-HBA) degradation reaction under UV-Vis irradiation.

2. EXPERIMENTAL

2.1. Materials

All reagents were of analytical grade and were used as received without further purification. The solutions were prepared with bi-distilled water.

2.2. Nanoparticles synthesis

A flowchart of the overall synthesis method is shown in Figure 1. A tin tetrachloride solution (Aldrich) diluted in a ratio of 2:5 in standard hydrochloride acid (37% HCl, Panreac), following a dilution up to a 0.1 M concentration was used as tin source. To this solution an ammonium 4 M solution (Merck) was added dropwise under vigorous stirring, until a complete precipitation of a white solid was observed. The resulting suspension was kept at rest for 15 hours at room temperature, and then filtered and vigorously rinsed with deionized water in order to remove the remaining ammonium and chloride ions. Crystallization of the SnO₂ precursor was done in autoclave at 200 °C, for 12 hours in aqueous suspension. The same chemical route was used to synthesize Co-doped SnO₂, by adding the required molar amount of metallic cobalt (Johnson Matthey) solubilized in nitric acid to the tin tetrachloride solution (doping step). After being washed, the undoped as well as the Co-doped SnO₂ nanoparticles can be easily stored in aqueous suspensions and straightforwardly retrieved by centrifugation whenever necessary. For this study, Sn_{1-x}Co_xO_{2-δ} samples with nominal Co/Sn ratios of $x = 0.005, 0.01, 0.03, 0.05, 0.10$ and 0.15 were prepared.

2.3. Photodegradation experiments

Adsorption studies were carried out using Sn_{1-x}Co_xO_{2-δ} nanoparticle suspensions in 4-HBA aqueous solution (10 ppm) under stirring in dark conditions. After centrifugation, the 4-HBA concentration was estimated by measuring the absorbance of its characteristic band centred at 248 nm.

The photodegradation experiments were conducted using a 250 ml refrigerated photo-reactor [29]. A 450 W Hanovia medium-pressure mercury-vapour lamp was used as radiation source, the total irradiated energy is 40-48% in the ultraviolet range and 40-43% in the visible region

of the electromagnetic spectrum. Suspensions were prepared by adding 30 mg of powder to 150 mL of a 10 ppm 4-HBA aqueous solution. Prior to irradiation, suspensions were stirred in darkness for 1 hour to ensure adsorption equilibrium. During irradiation, suspensions were sampled at regular intervals, centrifuged and analyzed by UV-vis spectroscopy.

2.4. Characterization

X-ray powder diffraction was performed using a Philips X-ray diffractometer (PW 1730) with automatic data acquisition (APD Philips v3.6B), using Cu K α radiation ($\lambda = 0.15406$ nm) and working at 40 kV/30 mA. The diffraction patterns were collected in the 2θ range of $20^\circ - 60^\circ$ with a 0.02° step size and an acquisition time of 2.0 s/step. The diffractometer was calibrated before every measurement, and the instrumental broadening (1.61×10^{-3} rad) was measured from a standard macrocrystalline and strain-free silicon sample. The $K\alpha_2$ contribution was removed before the XRD pattern analyses. The 2θ angular position of the diffraction peaks and their full-width at half-maximum, β , were calculated by fitting the experimental diffraction lines with a Pseudo-Voigt function. The β values were corrected taking into account the instrumental broadening. Transmission electron microscopy (TEM) and selected area electron diffraction (SAED) were carried out using a JEOL 200CX microscope operating at 200 kV. The elemental composition of the samples was analysed by energy dispersive X-ray spectroscopy (EDS). UV-VIS absorption spectra of the solutions were recorded using a UV-VIS absorption spectrophotometer (Shimadzu, UV-2600PC). The powder diffuse reflectance spectra (DRS) were recorded in the wavelength range of 220-1400 nm using the same equipment with an ISR 2600plus integration sphere.

3. RESULTS AND DISCUSSION

3.1. Structure and morphology

Figure 2 shows a representative set of diffractograms recorded for the synthesized undoped SnO₂ and Sn_{1-x}Co_xO_{2- δ} nanopowder samples. The diffraction reflections were indexed on the basis of the tetragonal rutile SnO₂ phase, using the JCPDS database card no. 41-1445 [3]. All the XRD patterns show broad peaks matching the expected diffraction reflections of the (110), (101), (200), (211) and (220) rutile SnO₂ planes, with similar relative intensities. No traces of other undesirable phases were observed throughout the whole range of Co contents considered, *e.g.* cobalt clusters, cobalt oxides, Co-Sn or Co-Sn-O phases, even when the diffracted intensity was plotted on a logarithmic scale. Note, however, that the presence of Co

in addition to Sn and O was confirmed for all Co-doped samples by EDS, with a Co:Sn ratio close to the nominal stoichiometry (not shown). Therefore, the XRD patterns seem to provide evidence for the homogeneous distribution of Co into the SnO₂ matrix, within the detection limit of the technique.

The effect of Co-doping on the structure of SnO₂ was studied by analysing the lattice parameters, the unit cell volume and the microstrain of the powder samples. Based on the interplanar distance, d_{hkl} , between the (hkl) planes of a tetragonal system, the lattice parameters of the different synthesized samples were calculated using the relations

$$\begin{cases} a = \sqrt{2} d_{110} \\ c = \frac{a d_{101}}{\sqrt{a^2 - d_{101}^2}} \end{cases}, \quad (1)$$

taking into account Bragg's law $d_{hkl} = \lambda/2 \sin \theta_{hkl}$ and the 2θ angular positions of the (110) and (101) peaks in the XRD patterns (Figure 2). The lattice parameters obtained as well as the unit cell volume ($V = a^2c$) are given in Table 1. While the a parameter increases almost linearly with increasing Co content, the c parameter has a maximum for $x = 0.03$. Nonetheless, the overall unit cell volume increases by about 0.34% when x increases from 0 to 0.15, as can be seen in Figure 3. This variation is related with the ionic radius size effect of Co²⁺ ($r = 0.745$ Å) when replacing Sn⁴⁺ ($r = 0.69$ Å) [30] into the SnO₆ octahedra SnO₂ building blocks, and consequent increase of oxygen vacancies due to the unbalanced electrical charge, which also causes cation repulsion and a unit cell volume increase. The samples' microstrain, ε , was evaluated using the formula

$$\varepsilon = \frac{d_{hkl} - d_{hkl}^s}{d_{hkl}^s}, \quad (2)$$

where d_{hkl}^s stands for the standard interplanar distance between the (hkl) planes. The ε values were estimated using the interplanar distance between the (110) planes, and are given in Table 1. As can be seen, the microstrain of all samples are positive (tensile strain), increasing from 0.011×10^{-3} to 1.759×10^{-3} with increasing Co content.

In what concerns the samples' mean crystallite sizes, $\langle D \rangle$, they were evaluated by Scherrer's equation [31] using the (110) reflections. The diffractograms of the different samples enabled to estimate $\langle D \rangle$ between 3.25 nm and 3.42 nm. These values are similar, and no correlation between the mean crystallite size and the samples' Co content could be deduced (see Table 1).

Given the above mentioned mean crystallites sizes and assuming spherically shaped particles, the number of unit cells per particle is only about 250.

The morphology and structure of the nanoparticle samples were further investigated by transmission electron microscopy. Figure 4 shows bright field TEM micrographs of a representative set of synthesised nanopowder samples as well as SAED images and the respective particle size histograms. As shown, the undoped SnO₂ sample is composed of nanoparticles showing a *quasi*-spherical shape, which can be made almost monodisperse by acidifying the particles' suspension with nitric acid (inset upper-left TEM micrograph). This result could probably be attributed to double layer repulsion phenomena, well known to be responsible for the stability of colloidal systems [32]. Since the sample consists of a very large number of small randomly distributed crystals, the SAED pattern consist of well-defined continuous diffraction rings, which can be indexed, from inside to outside, to the (110), (101), (200) and (211) planes of rutile SnO₂, in accordance with XRD reflections described above. The sample's particle size follows a lognormal distribution with mean size 3.82±1.06 nm, in good agreement with the size of the coherent diffracting domains calculated from the XRD pattern using Scherrer's equation. Analogous microstructures were found for the Co-doped samples. SAED images of each Co-doped samples are shown as insets in the corresponding TEM micrograph. The analysis of the TEM images show that Co-doped samples present similar spheroidal morphologies as found for the undoped samples, with particle sizes also following a lognormal distribution with mean values varying between 3.59±0.71 nm and 4.06±0.96 (see Table 1), in accordance with the $\langle D \rangle$ values found using XRD data. The SAED patterns of the Sn_{1-x}Co_xO_{2-δ} samples are comparable to that described above for the undoped sample.

3.2. UV-Vis spectroscopy

The optical characterization of the undoped and Co-doped SnO₂ samples was carried out by measuring their diffuse reflectance, R , at room temperature. R can be related to the absorption Kubelka-Munk function F_{KM} , by the relation $F_{KM}(R) = (1 - R)^2 / 2R$, which is proportional to the absorption coefficient [33]. The obtained absorption spectra are shown in Figure 5. A significant red shift in the optical absorption band edge can be seen for the Co-doped samples compared to the undoped sample. The optical bandgap energies of the samples, E_g , were estimated by plotting the function $f_{KM} = (F_{KM} h\nu)^2$ vs. $h\nu$ (Tauc plot), where h stands for Planck's constant and ν for the radiation frequency, and by extrapolating the linear portion of

the curve to zero absorption (Figure 6). The different extrapolated E_g values are given in Table 2. The optical bandgap of the undoped SnO₂ sample was estimated as 3.72 ± 0.03 eV which is blue shifted by 0.12 eV relative to the SnO₂ bulk value (3.6 eV). One may wonder if such blue shift might originate from the quantum confinement phenomenon associated with the nanosized crystallites that form the synthesized samples [34]. The structural size effect can be important if the crystallite size is in the range of the Bohr radius of the first excitonic state, which is given by [35]

$$r_B = \frac{m_0 \varepsilon_r}{\mu} a_B, \quad (3)$$

where m_0 stands for the electron mass, ε_r for the relative dielectric permittivity, μ for the effective reduced electron-hole mass, and a_B for the Bohr radius of the hydrogen atom (5.292×10^{-11} m). For the SnO₂, $\varepsilon_r = 14$, the electron effective mass is $m_e^* = 0.275 m_0$ and the hole effective mass is $m_h^* \ll m_e^*$ (i.e. $\mu \approx 0.275 m_0$) [36]. Computing these values in equation 3, we get $r_B = 2.7$ nm. Since $2r_B$ is greater than the average crystallite size of the undoped SnO₂ nanopowder sample (see Table 2), its optical behaviour can readily be ascribed to the effect of particle size. Note however that the E_g blue shift of this sample (0.12 eV) is lower than that we might expect (0.52 eV) using Brus' model [34]. The opposite behaviour was found for the optical bandgap energies of Co-doped SnO₂ samples. All doped samples present E_g values red shifted relative to the standard SnO₂ bulk value, despite having nanoparticle sizes similar to that determine for the undoped SnO₂ sample. Figure 7 shows the E_g values as a function of the Co content. As can be seen, the optical bandgap energies of the Sn_{1-x}Co_xO_{2-δ} samples decrease with increasing Co content, the E_g values sharply decreasing to 3.23 ± 0.08 eV for $x = 0.03$ before slowing down when approaching the lower limit of 3.19 ± 0.09 eV for $x = 0.15$. Similar narrowing of the optical bandgap has been reported in the literature for Co-doped SnO₂ [37-39] as well as for Fe-doped SnO₂ [40,41] nanopowders. Since the synthesis procedure for the Co-doped SnO₂ samples was similar to that used to synthesize the undoped samples, it can be concluded that the red shift deduced for the optical bandgap of the doped samples results from the Co doping process. Furthermore, this result seems to be consistent with the hypothesis that Co is homogeneously distributed in the substitutional sites of the SnO₆ octahedra tin oxide based structures, and thus gives rise to Sn_{1-x}Co_xO_{2-δ} doped structures with oxygen deficiency due to the lower valence states of cobalt compared to tin, as

previously mentioned. Indeed, the red shifts of Co-doped SnO₂ are consistent with the introduction of electronic states in the tin oxide bandgap associated with the 3*d* electrons of Co²⁺ cations and oxygen defects, in a similar way to what occurs in Co-doped TiO₂ [42], and for which band-structure calculations have shown that the valence band derives primarily from O 2*p*-levels, the conduction band from the Ti 3*d*-levels, and that the crystal-field split Co 3*d*-levels form localized bands within the original bandgap of TiO₂ [43-45]. The results reported here seem to support that comparable effects may occur when Co replaces Sn in the SnO₂ host lattice. The localized states induced by Co doping are expected to form tails of states that extend the bands into the bandgap, producing an absorption tail known as Urbach tail [46]. The Urbach energy, E_U , associated with the width of the Urbach tail obeys the exponential law [46]

$$\alpha = \alpha_0 e^{\frac{h\nu}{E_U}}, \quad (4)$$

where α is the optical absorption coefficient and α_0 is a constant. Since the absorption Kubelka-Munk function F_{KM} is proportional to the sample's absorption, the Urbach energies of the different synthesized samples were estimated from the slopes of $\ln(F_{KM})$ plotted as a function of photon energy, in an energy range just below the gap (not shown). The calculated E_U values as a function of the samples' Co content are plotted in Figure 8 and given in Table 2. As shown, E_U varies from 0.179 eV to 1.749 eV as x increases from 0 to 0.15, the higher E_U values indicating further introduction of tails into the bandgap of the Sn_{1-x}Co_xO_{2-δ} samples. This can be further highlighted by plotting E_g as a function of E_U , as shown in the inset of Figure 8. As the Urbach energy increases, the optical bandgap energy decreases, increasing the red shift due to possible band-to-tail and tail-to-tail transitions. Moreover, the optical bandgap decreases as the Urbach energy increases, with a fairly linear dependence, which reflects the influence of the structural disorder increase on the width of the absorption tail of the synthesized nanopowders as the Co content increases [47,48], in accordance with the increase of the samples' microstrain as previously discussed. Studies of the Urbach energies of SnO₂ are scarce in literature. A value of 0.037 eV was reported for single crystals of SnO₂ [49]. However, higher Urbach energies have already been found either for films or for particular SnO₂ based materials, mostly with amorphous or nanocrystalline phases. Melsheimer and Ziegler [50] studied the Urbach tail of SnO₂ thin films deposited by the spray pyrolysis technique, reporting E_U values of 0.220 eV for films deposited at 500 °C (polycrystalline films) and 0.530 eV for films deposited at 340 °C (amorphous films). More

recently Chetri and Choudhury [51] reported Urbach energies of 0.424 and 0.432 eV for SnO₂ nanoparticles annealed at 200 °C (crystallite size 2.53 nm) and 600 °C (crystallite size 6.45 nm), respectively. Regarding Co-doped SnO₂, Habubi *et al.* [52] reported E_U values of 0.512 eV and 0.588 eV for Co:SnO₂ films with 3% and 7% of cobalt, respectively, and crystallite sizes of about 50 nm.

3.3. 4-HBA photodegradation

The photocatalytic activity of the Sn_{1-x}Co_xO_{2-δ} nanopowders was studied using 4-HBA as model pollutant. Prior to photocatalysis, the adsorption ability of the samples was tested and it was found that after one hour in dark conditions no 4-HBA adsorption was noticed, either on the SnO₂ or on the Co doped-SnO₂ surfaces. The 4-HBA typical absorption spectrum is characterized by one broad absorption band centred at 248 nm, which is related with the absorption by the aromatic ring. This absorption peak was used as a reference for the photodegradation analysis.

Figure 9 shows the absorption spectra of a 10 ppm 4-HBA solution during irradiation in the presence of Sn_{0.95}Co_{0.05}O₂. A clear decrease of the 4-HBA characteristic 248 nm absorbance band intensity was observed with increasing irradiation time. Identical profile spectra were obtained for all the tested samples and for photolysis (not shown), which suggests an identical mechanism for the 4-HBA photocatalytic degradation process. A close inspection of the obtained absorption spectra (inset of Figure 9) shows, for early irradiation times, a decrease and a slight broadening of the 248 nm absorbance band. A simultaneous increase of the 270 - 315 nm absorption range arises. The broadening of the 248 nm absorbance band can be associated with the presence of benzoquinone (BQ), phenol, catechol (COH) and resorcinol (ROH), with maximum absorption peaks at 246, 270, 275 and 273 nm, respectively [53]. On the other hand the increase of the absorbance at 288 nm can be attributed to the presence of hydroquinone (HQ). This behaviour has been attributed to an initial and fast formation of the photodegradation's main byproducts (*e.g.* catechol, resorcinol, hydroquinone and benzoquinone) which absorb in the same 4-HBA wavelength range [53].

Figure 10 shows the 4-HBA absorption spectra obtained after 60 minutes of irradiation in the presence of the different SnO₂ based samples. As shown, either the undoped SnO₂ or the Co-doped SnO₂ powders have demonstrated photocatalytic activity on the 4-HBA degradation process. The best performance was obtained using nanoparticles with composition Sn_{0.95}Co_{0.05}O_{2-δ}. Indeed, after 60 min of irradiation no peaks related either to 4-HBA or to its

degradation byproducts appear in the final solution absorption spectrum. On the other hand, the sample with the lower photocatalytic ability for the 4-HBA degradation was the undoped SnO₂. Increasing Co doping up to 5%, a gradual improvement of the photocatalytic performance of SnO₂ was observed. Note, however, that for the sample with the highest Co-doping nominal amount (15%) a slight decrease of the photocatalytic activity resulted. This result suggests the existence of Co doping limit < 15% in order to optimize the photocatalytic activity of the Sn_{1-x}Co_xO_{2-δ} nanoparticles for the 4-HBA degradation.

4. CONCLUSIONS

A new and fast chemical route to synthesize single-phase Co-doped SnO₂ nanopowders was developed. It was shown that pure and highly stable Sn_{1-x}Co_xO_{2-δ} ($0 \leq x \leq 0.15$) nanoparticles can be synthesized under low temperature conditions, with mean grain sizes of about 3.5 nm and the dopant element homogeneously distributed in substitutional sites of the SnO₂ matrix. The microstrain of all samples are positive, increasing from 0.011×10^{-3} to 1.759×10^{-3} with increasing Co content. Consistently with *n*-type doping, the UV-visible diffuse reflectance spectra of representative powder samples have revealed red shifts, the optical bandgap energies decreasing with increasing Co concentration. The samples' Urbach energies were calculated and correlated with their bandgap energies. It was shown that the optical bandgap energy decreases, increasing the red shift due to possible band-to-tail and tail-to-tail transitions. Moreover, E_g linearly decreases with E_U , which reflects the influence of the increasing structural disorder on the width of the absorption tail of the synthesized nanopowders as the Co content increases, in accordance with the samples' microstrain variation.

The photocatalytic behaviour of the Sn_{1-x}Co_xO_{2-δ} nanopowders was investigated for the 4-HBA degradation process. The best 4-HBA photocatalyst was Sn_{0.95}Co_{0.05}O_{2-δ}. The complete photodegradation of a 10 ppm 4-HBA solution was achieved in 60 min, using 0.02% (w/w) of that material. Enhancement of the SnO₂ light absorption associated with an electron trapping phenomenon, which is a consequence of the Co-doping, is the most probable mechanism to explain these results.

Acknowledgements

This work was supported by Fundação para a Ciência e Tecnologia (FCT) under project No. PTCD/CTM/101033/2008. O.C. Monteiro acknowledges PEst-OE/QUI/UI0612/2013. The

authors thank P.I.C. Teixeira for critically reading of the manuscript.

References

1. S.W. Lee, Y.W. Kim and H. Chen, Electrical properties of Ta-doped thin films prepared by the metal–organic chemical vapor deposition method, *Appl. Phys. Lett.* 78 (2001) 350-352.
2. M.G. Mason, L.S. Hung, C.W. Tang, S.T. Lee, K.W. Wong and M. Wang, Characterization of treated indium–tin–oxide surfaces used in electroluminescent devices, *J. Appl. Phys.* 86 (1999) 1688-1692.
3. The International Centre for Diffraction Data®, JCPDF file no. 41-14445.
4. S. Chacko, N.S. Philip and V.K. Vaidyan, Effect of substrate temperature on structural, optical and electrical properties of spray pyrolytically grown nanocrystalline SnO₂ thin films, *Phys. Stat. Sol. (a)* 204 (2007) 3305-3315.
5. H.X. Yang, J.F. Qian, Z.X. Chen, X.P. Ai and Yu L. Cao, Multilayered nanocrystalline SnO₂ hollow microspheres synthesized by chemically induced self-assembly in the hydrothermal environment, *J. Phys. Chem C* 111 (2007) 14067-14071.
6. Z. Ying, Q. Wan, Z.T. Song and S.L. Feng, SnO₂ nanowhiskers and their ethanol sensing characteristics, *Nanotechnology* 15 (2004) 1682-1684.
7. X. Xu, J. Zhuang and X. Wang, SnO₂ quantum dots and quantum wires: controllable synthesis, self-assembled 2D architectures, and gas-sensing properties, *J. Am. Chem. Soc.* 130 (2008) 12527-12535.
8. F. Gyger, M. Hubner, C. Feldmann, N. Barsan and U. Weimar, Nanoscale SnO₂ hollow spheres and their application as a gas-sensing material, *Chem. Mater.* 22 (2010) 4821-4827.
9. H.L. Su, Q. Dong, J.Q. Xu and D. Zhang, Influence of hierarchical nanostructures on the gas sensing properties of SnO₂ biomorphic films, *Sensors and Actuators B: Chemical* 123 (2007) 420-428.
10. Y. Cheng, P. Xiong, C.S. Yun, G.F. Strouse, J. Zheng, R.S. Yang and Z.L. Wang, Mechanism and optimization of pH sensing using SnO₂ nanobelt field effect transistors, *Nano Lett.* 8 (2008) 4179-4184.
11. Y. Cheng, K.-S. Chen, N.L. Meyer, J. Yuan, L.S. Hirst, P.B. Chase and P. Xiong, Functionalized SnO₂ nanobelt field-effect transistor sensors for label-free detection of cardiac troponin, *Biosens. Bioelectron.* 26 (2011) 4538-4544.

12. K.L. Chopra, S. Major and D.K. Pandya, Transparent conductors - A status review, *Thin Solid Films* 102 (1983) 1-42.
13. F. Wagner, Transparent electronic, *Science* 300 (2003) 1245-1246.
14. S.J. Ding, J.S. Chen, G.G. Qi, X.N. Duan, Z.Y. Wang, E.P. Giannelis, L.A. Archer and X.W. Lou, Formation of SnO₂ hollow nanospheres inside mesoporous silica nanoreactors, *J. Am. Chem. Soc.* 133 (2011) 21-23.
15. D. Deng and J.Y. Lee, Hollow core-shell mesospheres of crystalline SnO₂ nanoparticle aggregates for high capacity Li⁺ ion storage, *Chem. Mater.* 20 (2008) 1841-1846.
16. M.S. Arnold, P. Avouris, Z.W. Pan and Z.L. Wang, Field-effect transistors based on single semiconducting oxide nanobelts, *J. Phys. Chem. B* 107 (2002) 659-663.
17. M.A. Hossain, J.R. Jennings, Z.Y. Koh and Q. Wang, Carrier generation and collection in CdS/CdSe-sensitized SnO₂ solar cells exhibiting unprecedented photocurrent densities, *ACS Nano* 5 (2011) 3172-3181.
18. J.Y. Liu, T. Luo, T.S. Mouli, F.L. Meng, B. Sun, M.Q. Li and J.H. Liu, A novel coral-like porous SnO₂ hollow architecture: biomimetic swallowing growth mechanism and enhanced photovoltaic property for dye-sensitized solar cell application, *Chem. Commun.* 46 (2010) 472-474.
19. P.R. Bueno, J.A. Varela and E. Longo, Admittance and dielectric spectroscopy of polycrystalline semiconductors, *J. Eur. Ceram. Soc.* 27 (2007) 4313-4320.
20. N. Kamiuchi, T. Mitsui, N. Yamaguchi, H. Muroyama, T. Matsui, R. Kikuchi and K. Eguchi, Activation of Pt/SnO₂ catalyst for catalytic oxidation of volatile organic compounds, *Catalysis Today* 157 (2010) 415-419.
21. S.B. Ogale, R.J. Choudhary, J.P. Buban, S.E. Lofland, S.R. Shinde, S.N. Kale, V.N. Kulkarni, J. Higgins, C. Lanci, J.R. Simpson, N.D. Browning, S. Das Sarma, H.D. Drew, R.L. Greene, T. Venkatesan, High temperature ferromagnetism with a giant magnetic moment in transparent Co-doped SnO_{2-δ}, *Phys. Rev. Lett.* 91 (2003) 077205-4.
22. Y. Matsumoto, M. Murakami, T. Shono, T. Hasegawa, T. Fukumura, M. Kawasaki, P. Ahmet, T. Chikyow, S. Koshihara and H. Koinuma, Room-temperature ferromagnetism in transparent transition metal-doped titanium dioxide, *Science* 291 (2001) 854-856.
23. L.C.J. Pereira, M.R. Nunes, O.C. Monteiro and A.J. Silvestre, Magnetic properties of Co-doped TiO₂ anatase nanopowders, *Appl. Phys. Lett.* 93 (2008) 222502-3.
24. K. Ueda, H. Tabata and T. Kawai, Magnetic and electric properties of transition-metal-doped ZnO films, *Appl. Phys. Lett.* 79 (2001) 988-990.
25. Photocatalysis. Science and Technology, M. Kaneko and I. Okura (Eds.), Biological and

- Medical Physics Series, Springer, Berlin, 2010.
26. R. Abe, M. Higashi, K. Sayama, Y. Abe and H. Sugihara, Photocatalytic activity of R_3MO_7 and $R_2Ti_2O_7$ ($R = Y, Gd, La; M = Nb, Ta$) for water splitting into H_2 and O_2 , *J. Phys. Chem. B* 110 (2006) 2219-2226.
 27. J. Hays, A. Punnoose, R. Baldner, M.H. Engelhard, J. Peloquin and K.M. Reddy, Relationship between the structural and magnetic properties of Co-doped SnO_2 nanoparticles, *Phys. Rev. B* 72 (2005) 075203-7.
 28. K. Tang, J. Zhang, W. Yan, Z. Li, Y. Wang, W. Yang, Z. Xie, T. Sun and H.J. Fuchs, One-step controllable synthesis for high-quality ultrafine metal oxide semiconductor nanocrystals via a separated two-phase hydrolysis reaction, *J. Am. Chem. Soc.* 130 (2008) 2676-2780.
 29. R. Albuquerque, M.C. Neves, M.H. Mendonça, T. Trindade, O.C. Monteiro, Adsorption and catalytic properties of SiO_2/Bi_2S_3 nanocomposites on the methylene blue photodecolorization process, *Colloid Surface A* 328 (2008) 107-113.
 30. R.D. Shannon, Revised effective ionic radii and systematic studies of interatomic distances in halides and chalcogenides, *Acta Crystallogr. A* 32 (1976) 751-767.
 31. B.D. Cullity, S.R. Stock, *Elements of X-ray Diffraction*, 3rd ed., Prentice Hall, N.J., 2001.
 32. K.J. Mysels and M.N. Jones, Direct measurement of the variation of double-layer repulsion with distance *Discuss. Faraday Soc.* 42 (1966) 42-50.
 33. G. Kortuem, *Reflectance spectroscopy: principles, methods and applications*, Springer-Verlag, New York, 1969.
 34. L. Brus, Electronic wave functions in semiconductor clusters: experiment and theory *J. Phys. Chem.* 90 (1989) 2555-2560.
 35. M. Fox, *Optical Properties of Solids*, Oxford University Press, Oxford, 2010, p. 78.
 36. E.J.H. Lee, C. Ribeiro, T.R. Giraldi, E. Longo, E.R. Leite and J.A. Varela, Photoluminescence in quantum-confined nanocrystals: evidence of free exciton decay, *Appl. Phys. Lett.* 84 (2004) 1745-1747.
 37. S. Ghosh, D.D. Munshi and K. Mandal, Paramagnetism in single-phase $Sn_{1-x}Co_xO_2$ dilute magnetic semiconductors, *J. Appl. Phys.* 107 (2010) 123919-5.
 38. L.M. Fang, X.T. Zu, Z.J. Li, S. Zhu, C.M. Liu, L.M. Wang and F. Gao, Microstructure and luminescence properties of Co-doped SnO_2 nanoparticles synthesized by hydrothermal method *J. Mater. Sci.: Mater. Electron.* 19 (2008) 868-874.
 39. K. Srinivas, M. Vithal, B. Sreedhar, M.M. Raja and P.V. Reddy, Structural, optical, and

- magnetic properties of nanocrystalline Co-doped SnO₂ based diluted magnetic semiconductors, *J. Phys. Chem. C* 113 (2009) 3543-3552.
40. G.A. Alanko, A. Thurber, C.B. Hanna, A. Punnoose, Size, surface structure, and doping effects on ferromagnetism in SnO₂, *J. App. Phys.* 111 (2012) 07C321-3.
 41. S. Ghosh, M. Mandal and K. Mandal, Effects of Fe doping and Fe–N-codoping on magnetic properties of SnO₂ prepared by chemical co-precipitation, *J. Mag. Mag. Mater.* 323 (2011) 1083-1087.
 42. S. Rout, N. Popovici, S. Dalui, M.L. Paramês, R.C. da Silva, A.J. Silvestre and O. Conde, Phase growth control in low temperature PLD Co:TiO₂ films by pressure, *Curr. Appl. Phys.* 13 (2013) 670-676.
 43. M.S. Park, S.K. Kwon, B.I. Min, Electronic structures of doped anatase TiO₂: Ti_{1-x}M_xO₂ (M = Co, Mn, Fe, Ni), *Phys. Rev. B* 65 (2002) 161201-161204.
 44. S.-D. Mo and W.Y. Ching, Electronic and optical properties of three phases of titanium dioxide: rutile, anatase, and brookite, *Phys. Rev. B* 51 (1995) 13023-13032.
 45. M.G. Ha, E.D. Jeong, M.S. Won, H.G. Kim, H.K. Pak, J.H. Jung, B.H. Shon, S.W. Bae, J.S. Lee, electronic band structure and photocatalytic activity of M-doped TiO₂ (M = Co and Fe), *J. Korean Phys. Soc.* 49 (2006) S675-S679.
 46. F. Urbach, The long-wavelength edge of photographic sensitivity and of the electronic absorption of solids, *Phys. Rev.* 92 (1953) 1324.
 47. G.D. Cody, T. Tiedje, B. Abeles, B. Brooks and Y. Goldstein, Disorder and the optical-absorption edge of hydrogenated amorphous silicon, *Phys. Rev. Lett.* 47 (1981) 1480-1483.
 48. J. Melsheimer and D. Ziegler, Band gap energy and Urbach tail studies of amorphous, partially crystalline and polycrystalline tin dioxide, *Thin Solid Films* 129 (1985) 35-47.
 49. M. Nagasawa and S. Shionoya, Temperature dependence of the fundamental optical absorption edge in stannic oxide, *J. Phys. Soc. Jpn.* 30 (1971) 1118-1123.
 50. J. Melsheimer and D. Ziegler, Band gap energy and Urbach tail studies of amorphous, partially crystalline and polycrystalline tin dioxide, *Thin Solid Films* 129 (1985) 35.
 51. P. Chetri and A.Choudhury, Investigation of optical properties of SnO₂ nanoparticles, *Physica E* 47 (2013) 257-263.
 52. N.F. Habubi, K.A. Mishjil and S.S. Chiad, Structural properties and refractive index dispersion of cobalt doped SnO₂ thin films, *Indian J. Phys.* 87 (2013) 235-239.
 53. M.C. Neves, J.M.F. Nogueira, T. Trindade, M.H. Mendonça, M.I. Pereira, O.C. Monteiro, Photosensitization of TiO₂ by Ag₂S and its catalytic activity on phenol

photodegradation, J. Photochem. Photobiol. A: Chem 204 (2009) 168-173.

Table captions

Table 1 – Lattice parameters, unit cell volume, microstrain and crystallite size of the different nanopowders synthesized.

Table 2 – Optical bandgap energies and Urbach energies of the different nanopowders synthesized.

Figure captions

Figure 1 – Flowchart of the synthesis method developed to prepare either SnO₂ or Co-doped SnO₂ nanoparticles.

Figure 2 – X-ray diffraction patterns of the undoped SnO₂ and Sn_{1-x}Co_xO_{2-δ} nanopowder samples.

Figure 3 – Unit cell volume of the Sn_{1-x}Co_xO_{2-δ} nanopowders as a function of the samples' Co content. Note that the unit cell volume increases by only 0.34% when the Co/Sn ratio increases by 15%.

Figure 4 – TEM micrographs of undoped SnO₂ and Sn_{1-x}Co_xO_{2-δ} nanopowder samples with $x = 0.05, 0.10$ and 0.15 , and the corresponding particle size distribution histograms. The inset at the upper-right corner of each TEM micrograph shows the corresponding SAED image.

Figure 5 – Diffuse reflectance spectra of the undoped SnO₂ and Sn_{1-x}Co_xO_{2-δ} nanopowder samples.

Figure 6 – Tauc plots of the undoped SnO₂ and different Sn_{1-x}Co_xO_{2-δ} samples. The optical bandgap energies were estimated by extrapolating the linear portion of the curve to zero absorption.

Figure 7 – Samples' optical bandgap energy vs. Co content. The dashed line is just a guide for the eye.

Figure 8 – Urbach energy vs. samples' Co content. The dashed line is just a guide for the eye. The inset shows the samples' optical bandgap energies as a function of their Urbach energy.

Figure 9 – Absorption spectra of a 4-HBA 10 ppm solution using 30 mg of Sn_{0.995}Co_{0.005}O_{2-δ} powder as photocatalyst, for different irradiation times. The inset shows a detail of the spectra in the 200 – 340 nm range. The peak positions of the main 4-HBA photodegradation byproducts are also shown (vertical dotted lines).

Figure 10 – Absorption spectra of a 10 ppm 4-HBA solution using different powder samples as photocatalyst, for 60 minutes of irradiation: a) photolysis, b) SnO₂, c) Sn_{0.995}Co_{0.005}O_{2-δ}, d) Sn_{0.99}Co_{0.01}O_{2-δ}, e) Sn_{0.97}Co_{0.03}O_{2-δ}, f) Sn_{0.95}Co_{0.05}O_{2-δ} and g) Sn_{0.85}Co_{0.15}O_{2-δ}.

Table 1

Sample	Nominal composition	Lattice parameters			Microstrain ^a ($\times 10^{-3}$)	Crystallite size (nm)	
		<i>a</i> (Å)	<i>c</i> (Å)	Cell volume (Å ³)		Scherrer ^b	TEM ^c
A	SnO ₂	4.7334	3.1861	71.3849	0.011	3.25	3.82±1.06
B	Sn _{0.995} Co _{0.005} O _{2-δ}	4.7356	3.1879	71.4898	0.465	3.42	3.59±0.71
C	Sn _{0.99} Co _{0.01} O _{2-δ}	4.7361	3.1896	71.5467	0.587	3.30	3.65±0.77
D	Sn _{0.97} Co _{0.03} O _{2-δ}	4.7369	3.1899	71.5757	0.749	3.27	3.91±0.73
E	Sn _{0.95} Co _{0.05} O _{2-δ}	4.7395	3.1871	71.5905	1.289	3.18	4.04±1.06
F	Sn _{0.90} Co _{0.10} O _{2-δ}	4.7391	3.1892	71.6272	1.211	3.34	4.06±0.96
G	Sn _{0.85} Co _{0.15} O _{2-δ}	4.7417	3.1857	71.6270	1.759	3.21	3.98±0.90

^a Values calculated using the interplanar distance between the (110) planes.

^b Values calculated from XRD data using Scherrer equation.

^c Values calculated from TEM image analyses.

Table 2

Sample	Nominal composition	E_g (eV)	E_U (eV)
A	SnO ₂	3.72±0.03	0.179±0.001
B	Sn _{0.995} Co _{0.005} O _{2-δ}	3.44±0.07	0.555±0.014
C	Sn _{0.99} Co _{0.01} O _{2-δ}	3.39±0.03	0.718±0.006
D	Sn _{0.97} Co _{0.03} O _{2-δ}	3.21±0.03	1.226±0.049
E	Sn _{0.95} Co _{0.05} O _{2-δ}	3.23±0.08	1.659±0.057
F	Sn _{0.90} Co _{0.10} O _{2-δ}	3.21±0.08	1.678±0.057
G	Sn _{0.85} Co _{0.15} O _{2-δ}	3.19±0.09	1.749±0.037

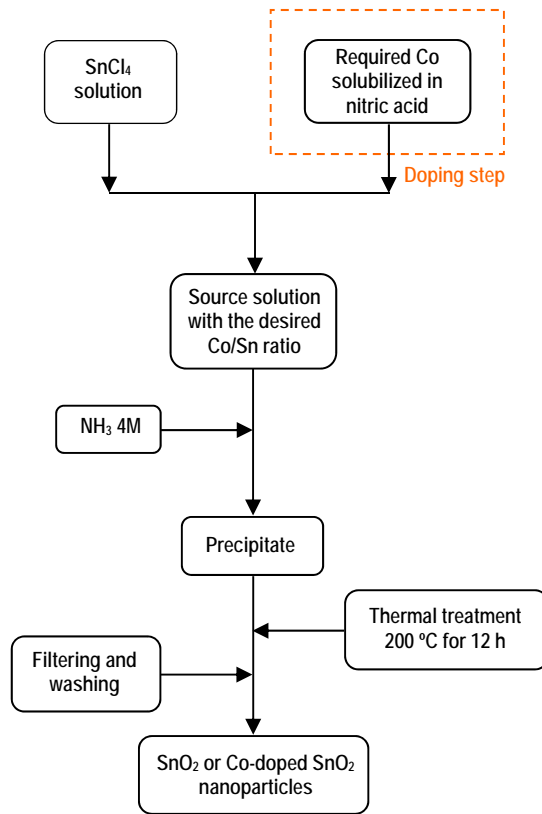


Figure 1

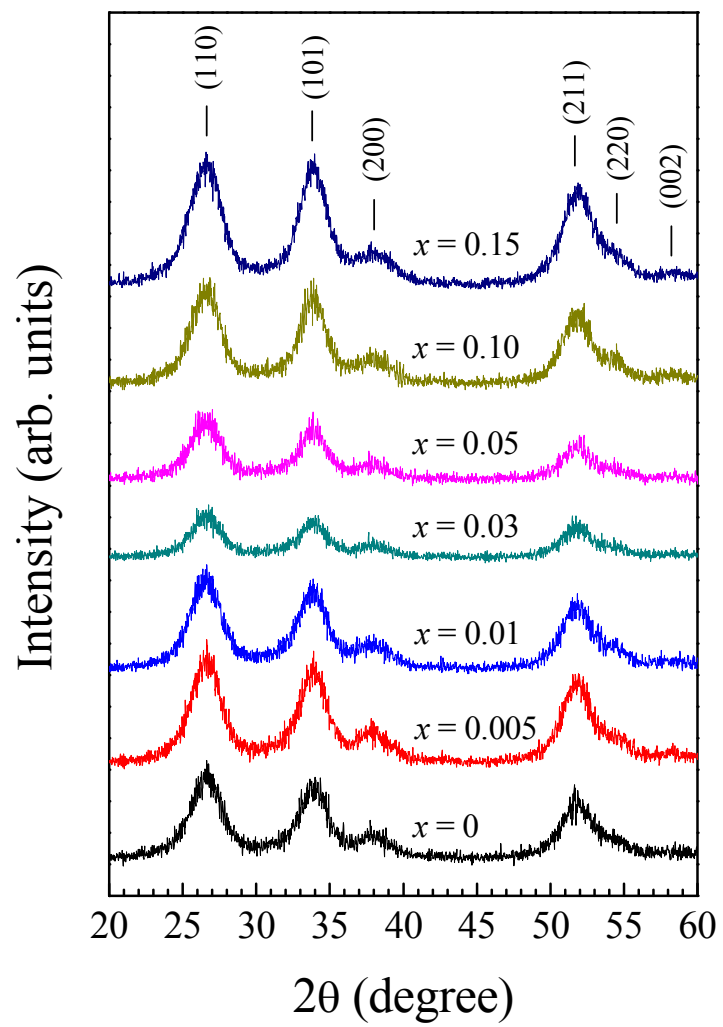


Figure 2

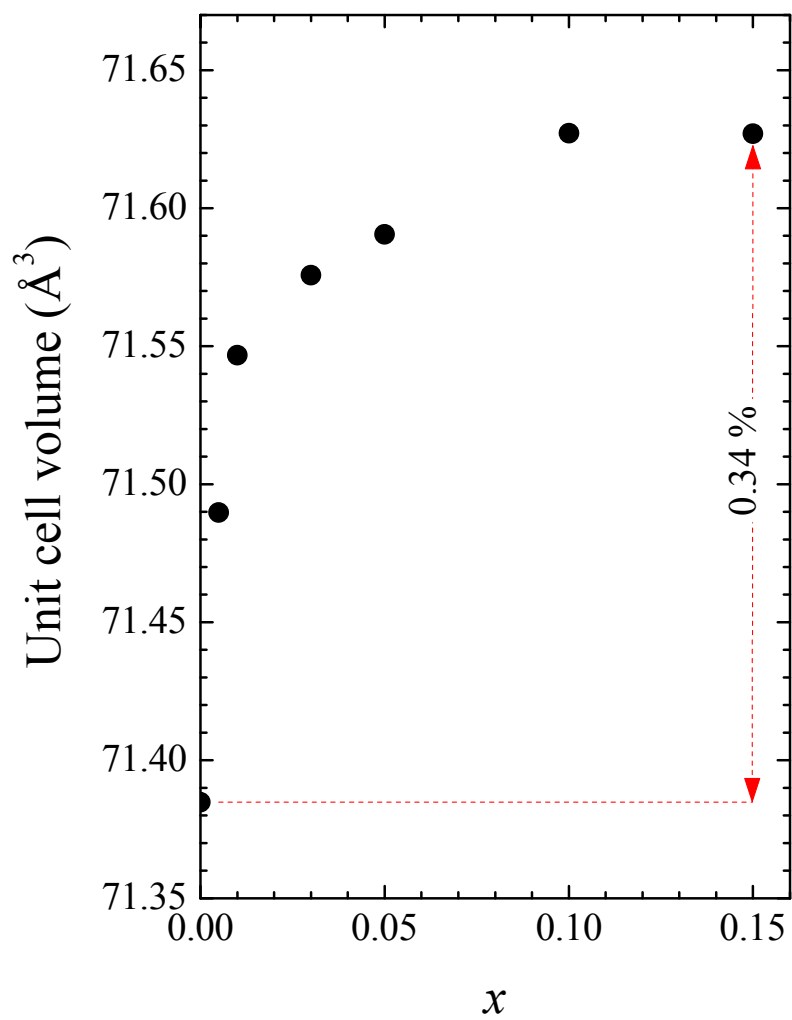


Figure 3

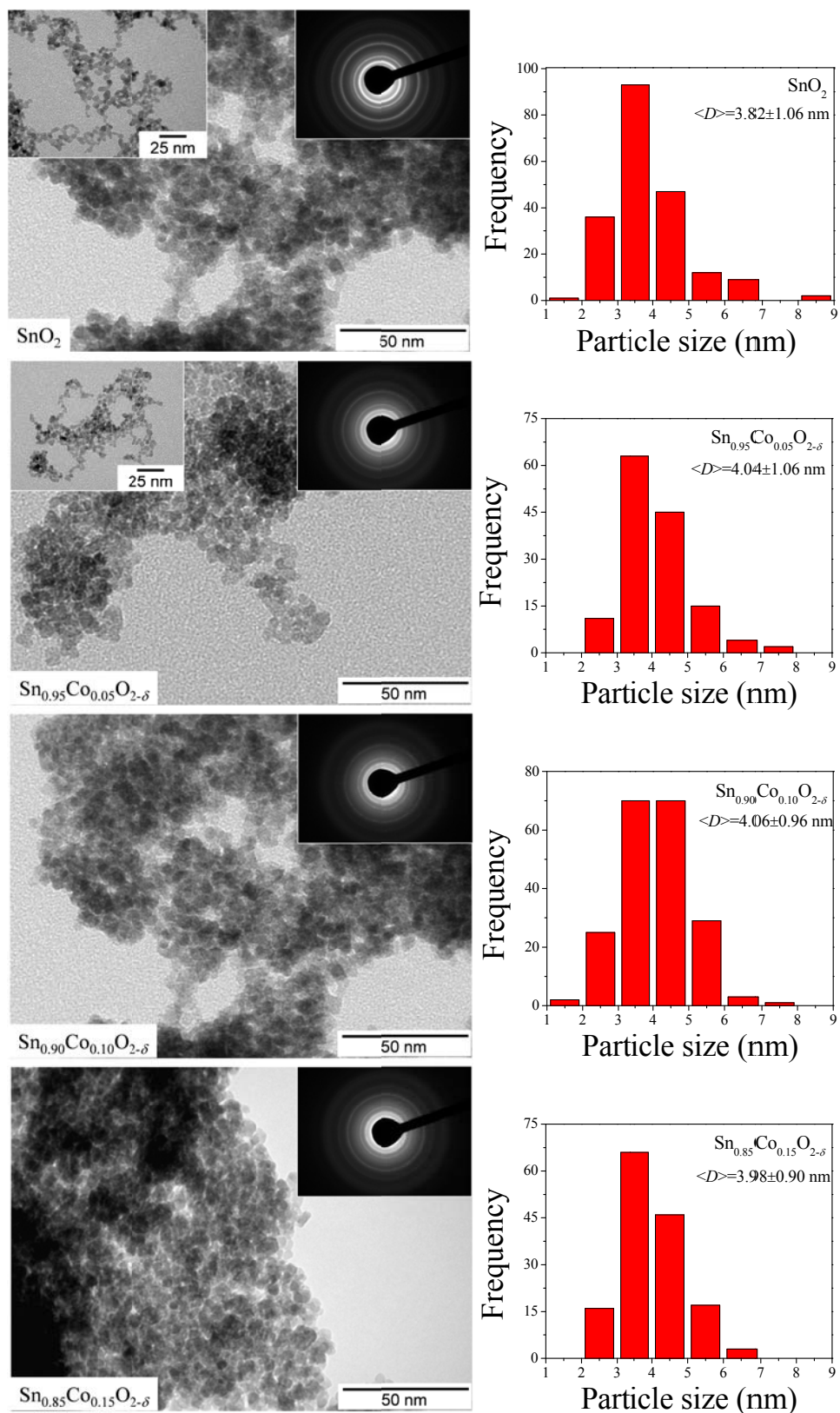


Figure 4

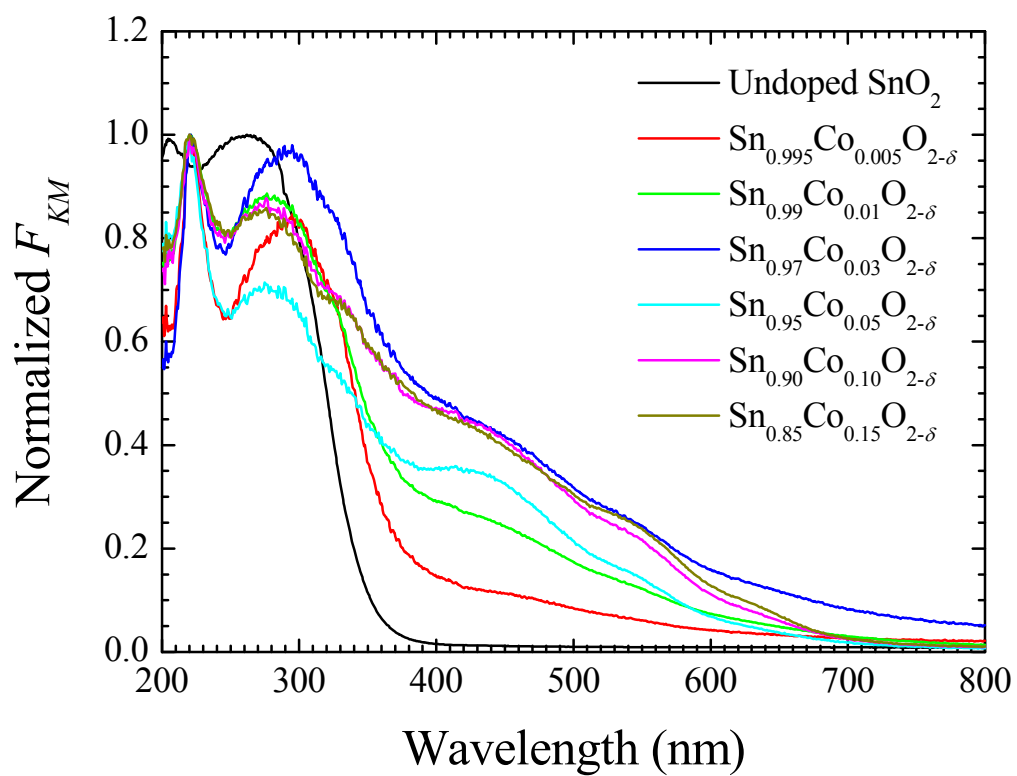


Figure 5

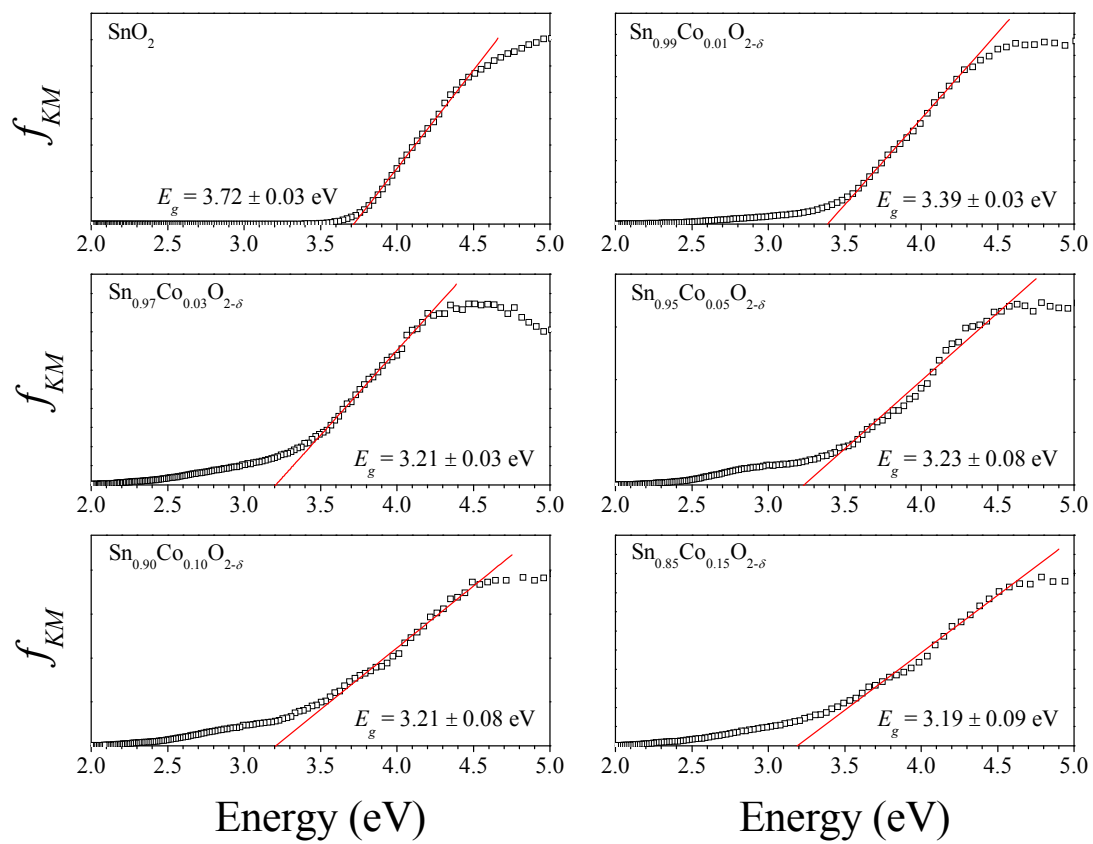


Figure 6

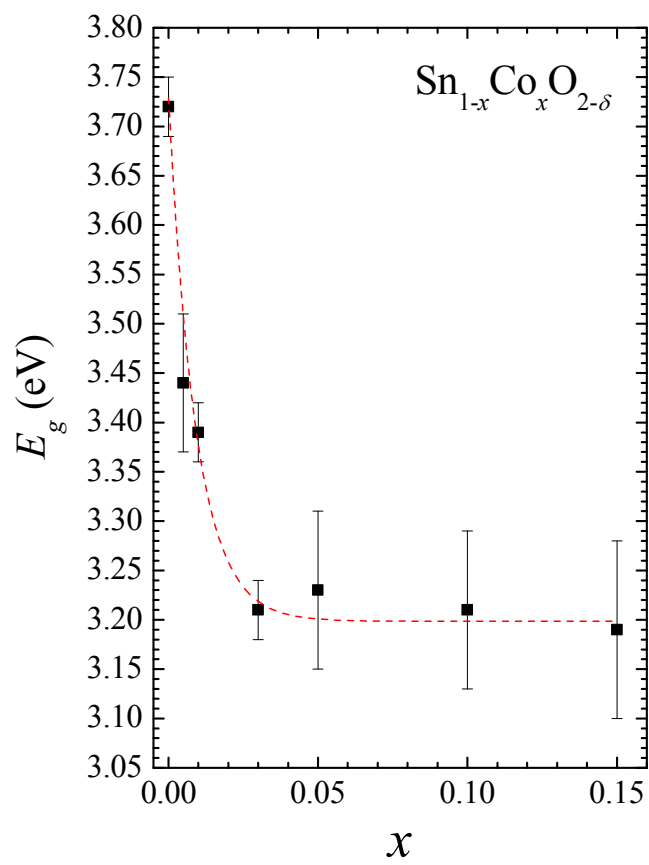


Figure 7

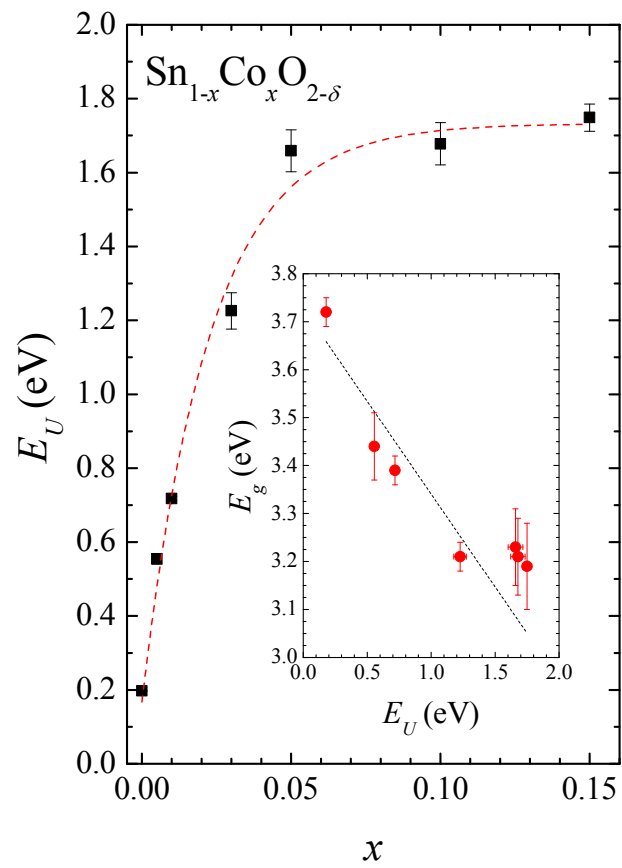


Figure 8

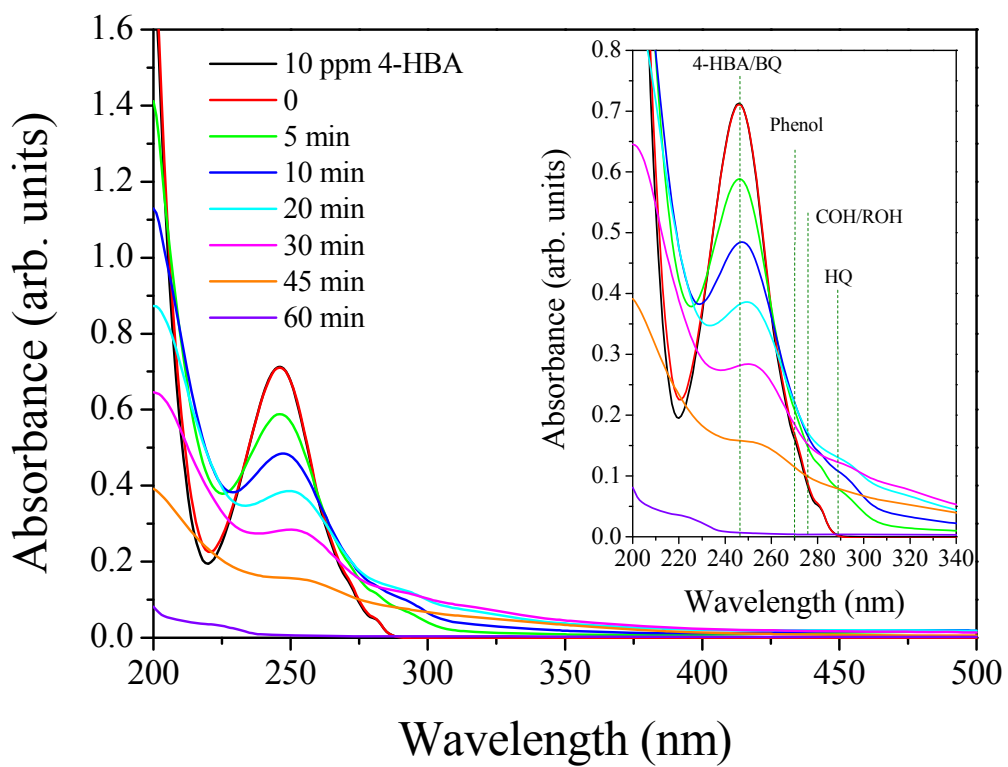


Figure 9

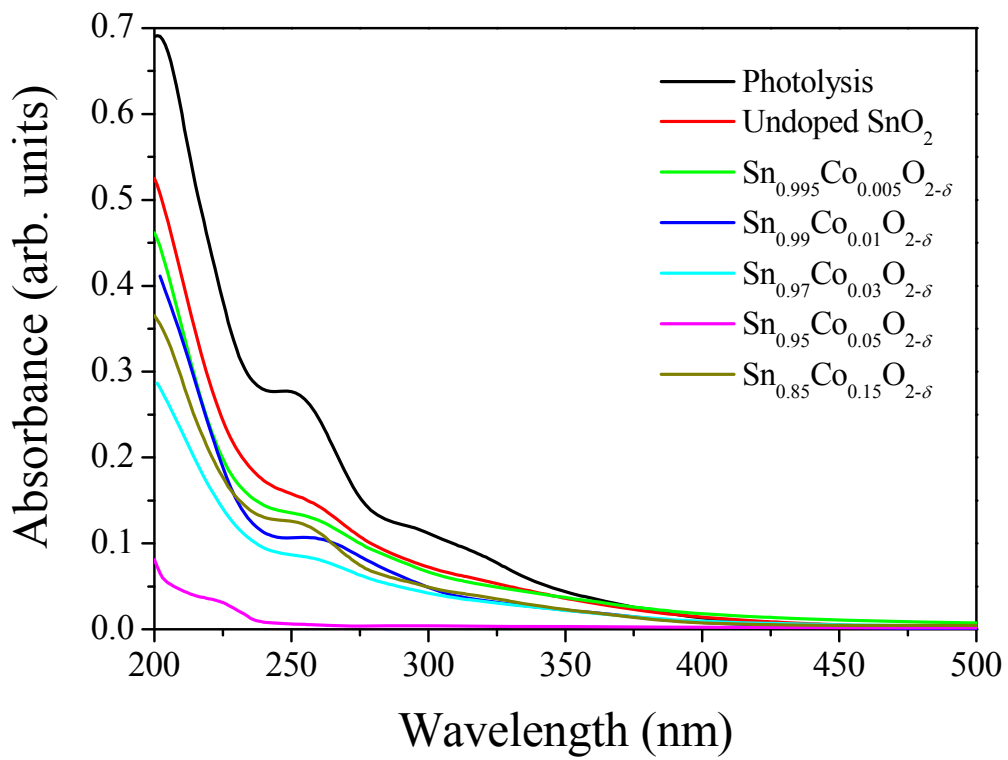


Figure 10